Design of Variable-Stiffness Morphing Skins Using Curvilinear Continuous Fibre 3D Printing

Chen Wang[a,*], Ziyi He[a], Yu Zhang[a], Xing Shen[a], Jiaying Zhang[b], Yuying Xia[c], Hamed Haddad Khodaparast[c], Michael I. Friswell[c]

[a] College of Aerospace Engineering, Nanjing University of Aeronautics and Astronautics
[*] Corresponding author: cwangaero@nuaa.edu.cn
[b] School of Aeronautic Science and Engineering, Beihang University
[c] Faculty of Science and Engineering, Swansea University

Abstract: A morphing skin must withstand local aerodynamic loads while remaining flexible enough to accommodate the shape changes of the morphing aircraft. The conflicting requirements can be satisfied by tuning the mechanical properties of the variable stiffness composites. In the present study, the variable stiffness composite is investigated by varying the lamina angles through 3D printing of curvilinear continuous fibre. At first, the design requirements and application scenario are introduced. The fabrication method is introduced and tensile tests are also performed to obtain the mechanical properties of the printed composite lamina. Then, the numerical model is established to explore the mechanical properties of the variable stiffness composite. Optimisation is carried out to balance the different mechanical properties. Finally, a composite sample is manufactured, which is tested to validate the proposed concept. The results demonstrate that the variable stiffness composite exhibits significant improvements in mechanical properties compared with the straight fibre composite.

Keywords: morphing skin; morphing aircraft; variable stiffness composite; continuous fibre 3D printing; structural optimisation

1. Introduction

Morphing aircraft can adaptively change their shape according to varying flight conditions. The structure of the morphing aircraft needs to carry the aerodynamic loads, and change the aerodynamic shape with limited actuation forces [1, 2]. The morphing skin, which needs to maintain the aerodynamic surface of the morphing structure, is one of the most challenging structural components for morphing aircraft. The morphing skin is expected to allow for the shape-changing of the inner structures without structural failure while withstanding local aerodynamic forces. These multiple requirements make it difficult to design and manufacture a promising morphing skin and indicate that the stiffness of the morphing skin should be tuned according to the load conditions: when the morphing skin is subject to aerodynamic loads, the stiffness should be high; but when it is subject to actuation loads, the stiffness should be low.

Different design approaches have been proposed to satisfy the requirements. According to the approach used to tune the stiffness, the morphing skin can be categorised into two main types[3, 4]. One approach is to change the skin stiffness adaptively based on the properties of the skin material or structure itself. Smart materials and structures are often applied in this design approach [5]. Shape memory polymers can endure a high failure strain and tune the stiffness actively, which makes it suitable for use as the skin [6, 7]. However, the stiffness of the polymer is relatively low, which requires additional reinforcement, such as cellular structures [8]. Pressure actuation can be also applied to tune the stiffness by changing the internal pressure of cellular structures [9-11]. Active tuning requires additional power and control systems, which will make the aircraft more complex and expensive.

The other approach is to make the skin structure anisotropic and tailor the skin stiffness based on the load conditions. In this approach, flexible structures based on cellular structures [12-14] and corrugated structures [15-18] are often applied as the inner supporting structures for the skin panel and polymers are often used as the skin surface. Stiffness tailoring can also be achieved via the design of composite structures. In the morphing leading edge structure, the stiffness of the morphing skin can be changed by varying the composite thickness [19, 20] or the lamina angle [21, 22]. By varying the stiffness in the morphing leading edge, it was found that the target shape of morphing structures could be achieved more effectively.

Compared to the variable stiffness composite based on the thickness variation, changing the lamina angle spatially can lead to an enlarged design space for the composites. Variable stiffness composites based on curvilinear fibre angle have been proposed for over three decades and applied to improve the stiffness distribution, and other performance measures, such as improving buckling performance [23, 24]. Different manufacturing methods, such as automated fibre placement and continuous tow shearing, have been investigated [25-27]. However, the requirements of manufacturing facilities and the costs of materials have limited the application of curvilinear fibre angle composites. In recent years, the fast development of 3D printing technology has provided new insights and research on curvilinear fibre angle composites [28, 29]. The 3D printer will usually have one nozzle to extrude the continuous fibre material, and another nozzle to extrude the matrix material. The continuous fibre material can be made of carbon, glass, etc. and can be pre-impregnated or used dry before being extruded into the composite. For the matrix material, thermoplastic materials, such as PLA, ABS and PETG, are widely used. Commercial 3D printers, such as the products from Markforged® [30] and Anisoprint® [31], have been applied in research, as well as custom-made 3D printers, such as those reported in [32].

With the continuous fibre applied as reinforcement in the matrix, the mechanical properties of the printed sample can be tuned. For example, Dong et al. [33] proposed a hybrid continuous fibre reinforced structure, which used 3D printing technology to embed the continuous fibre into the lattice structure to improve the compressive strength and stiffness. Sugiyama et al. [34] used the 3D printing of continuous fibre composites to manufacture sandwich structures, which increased the design flexibility of the sandwich core and showed the potential of tuning the mechanical properties. Cheng et al. [35] gave a review of 3D printing of continuous fibre composites in the field of lightweight structures. Lattice structures, cellular structures, and sandwich structures have been widely investigated to improve their mechanical properties. Furthermore, if shape memory polymers are used as the matrix material, the concept of 3D printing can be extended to 4D printing [36], which enables the composite to have active shape-changing capability. Wang et al. [37] applied continuous fibre reinforced composites in an origami structure and achieved active control of the structure. A 3D printer was used to manufacture the structure, which integrated the shape memory polymer as the matrix and the continuous carbon fibre as the reinforcement.

Although significant progress has been made in developing variable stiffness composites, curvilinear fibre designs, and 3D-printed continuous fibre structures, their direct application to morphing skins remains underexplored. Most existing studies have focused on enhancing stiffness distribution, buckling resistance, or lightweight structural performance, yet the challenge of creating a morphing skin that is both flexible and load-bearing has not been fully addressed. To date, little research has applied continuous fibre composite 3D printing to morphing skins. Heeb et al. [38] proposed multi-material 3D printing to manufacture a morphing skin, which relied on the different mechanical properties of thermoplastic rubber, but no continuous fibres were embedded as reinforcement. In the authors' earlier research [39], a curvilinear fibre composite was applied in a chordwise morphing wing design; however, the skin was neither manufactured nor experimentally tested. With the rapid development of 3D printing technology for continuous fibre composites, further research into morphing skins is both feasible and necessary.

In this paper, the concept of a morphing skin was introduced, and the potential of 3D printed continuous fibre composites in its design and validation were explored. Printed samples were manufactured to characterise the composite lamina properties, and these data were used to establish a finite element model of the morphing skin. A parametric study was then conducted, followed by optimisation to meet the design requirements. Finaly, the optimised morphing skin was manufactured, experimentally tested, and compared with samples reinforced by straight fibres, demonstrating the benefits of the proposed approach.

2. Model Definition

2.1 Conceptual Design of the Morphing Skin

In the present study, the morphing skin is intended for one-dimensional morphing designs, such as variable-chord and morphing camber wings. Figure 1 shows one potential application scenario of the proposed morphing skin, in which the morphing skin is designed to change the wing chord when subject to an actuation force.

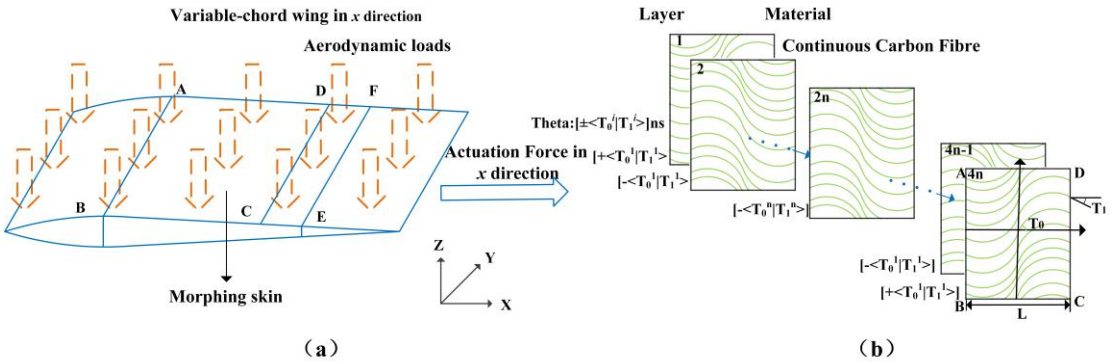

Fig. 1 (a) Morphing skin in the morphing wing (b) Variable lamina angle in the morphing skin

The composite morphing skin must withstand in-plane and out-of-plane loads. The morphing skin panel is simplified as a composite plate, as shown in Fig. 1(b), where morphing occurs along the x direction. The curvilinear fibre angle is denoted by θ, and the spanwise length of the skin panel is denoted as L. Considering the limitations of the 3D printer, the following linear equation is used to express the fibre lamina angle as [39]

$$\theta(x) = T_0 + 2(T_1 - T_0)\left|\frac{x}{L}\right| \tag{1}$$

where T_0 is the lamina angle at the mid-point of the composite plate (when x =0), T_1 is the lamina angle at the plate edges (when $x = \pm L/2$).

The fibre orientation is controlled by the parameters T_0 and T_1. The format $<\pm T_0|T_1>$ is used to represent the fibre path of the single ply layer. Figure 2 shows the different fibre paths when different combinations of the parameters T_0 and T_1 are adopted.

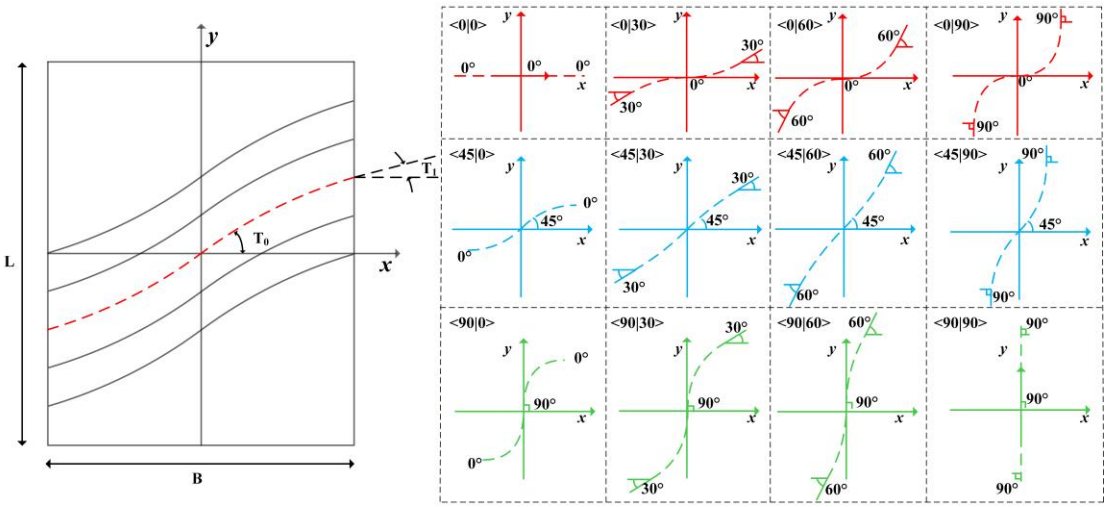

Fig. 2 The effect of T_0 and T_1 on the fibre path

2.2 Performance Requirement and Corresponding Index

As the morphing skin is designed for a one-dimensional application, one end of the morphing skin is fixed, and the other end is free to move along the morphing direction. The skin is subjected to both in-plane actuation forces and out-of-plane aerodynamic loads. Two load cases are considered in the current study. The first load case is the in-plane tension, which requires a small in-plane stiffness to reduce the actuation force. In the other load case, the skin is subject to out-of-plane loads, which requires a high out-of-plane stiffness to reduce the out-of-plane deformation. The boundary

conditions and loads of the morphing skin are shown in Fig. 3. Numerical simulation, optimisation and experimental study of these two working conditions will be performed in the following sections.

A skin with ±45° symmetrical straight fibres is used as the baseline design to non-dimensionalise the required actuation forces F, the maximum out-of-plane deformation U, with subscript b denoting the result of the baseline design. Thus, the non-dimensionalised indices can be represented as

$$\overline{F}=\frac{F}{F^b}$$
$$\overline{U}=\frac{U}{U^b} \tag{2}$$

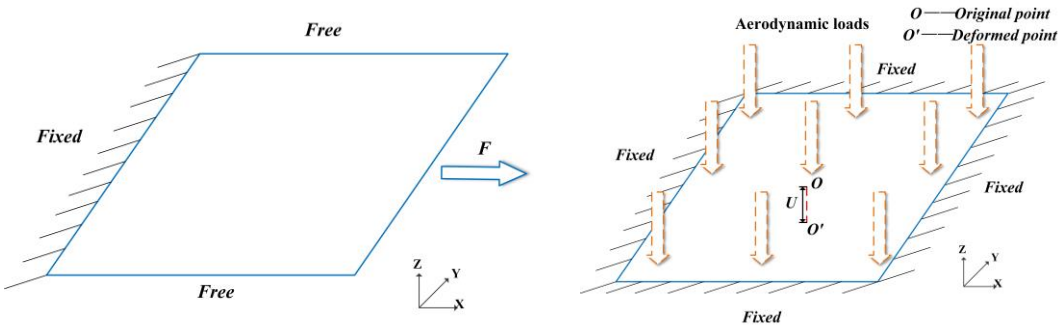

（a） （b）

Fig. 2 Boundary conditions and loads of the morphing skin: (a) In-plane tension (b) Out-of-plane deformation

3. Fabrication Method and Mechanical Properties

3.1 Fabrication Method based on 3D Printing

The composite samples are manufactured using the Anisoprint Composer A4 3D printer [40], which has a maximum printing size of 297 mm×210 mm×140 mm, as shown in Fig. 4. The printer can manufacture continuous fibre reinforced composites via the co-extrusion of both the continuous fibre and the matrix material.

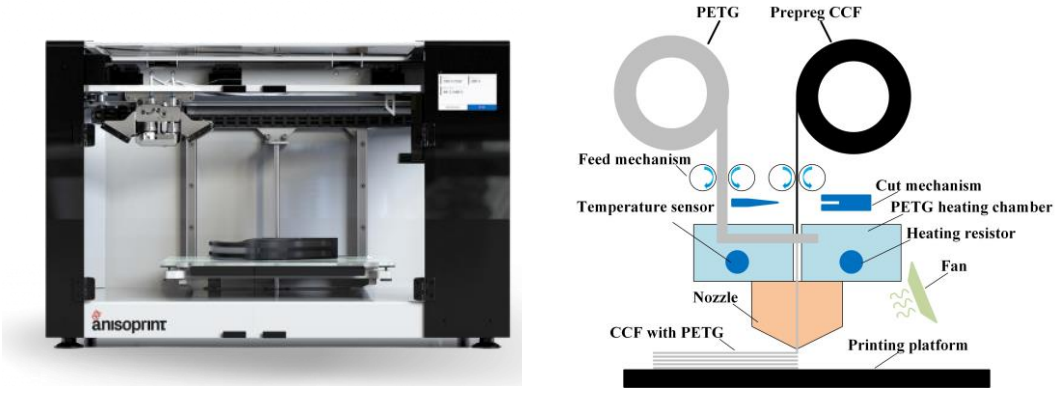

(a) (b)

Fig. 3 (a) 3D printer used in the study, (b) Schematic of the CCF technology

In the present study, the matrix material is polyethylene terephthalate glycol (PETG) which has a Young's modulus of around 1.12 GPa and the continuous carbon fibre (CCF) is used as the fibre

material. The PETG filament is fed into the printing head and melted, which is then extruded together with the carbon fibre filament. The carbon fibre is pre-impregnated and has a Young's modulus of around 149 GPa with a carbon fibre volume of around 60%.

A few factors, such as the printing speed, the nozzle temperature, and the environmental temperature affect the printing process, which will lead to different mechanical properties [41, 42]. Since the focus of the current study is the variable stiffness caused by the variable lamina angle of the fibre, the printing conditions are kept unchanged when different composite samples are manufactured. During manufacturing, the nozzle temperature was set to 235°C and the printing speed was set to 180 mm/min with the environmental temperature around 20°C. The samples were printed after the corresponding G-code source file is provided to the printer, and the change of the lamina angle is achieved by editing the G-code file of the printing sample.

With the co-extrusion of the fibre and matrix filament, a composite lamina similar to a unidirectional composite lamina can be manufactured. However, there are some differences between the composite plate made by the 3D printer and the one made by conventional methods. For example, due to the constraint of the 3D printer nozzle, there would be no fibre is deposited at the plate corners, if the size of the corner is too small. Also, the fibre remained continuous in the same lamina at the edge of the sample, until the 3D printer began to print the next layer. Since the focus is on the effect of the lamina angle, classic composite mechanics [43] is adopted in the current investigation, and the differences between the 3D printed composite and the classical composite will be examined in a future study.

3.2 Tests of Mechanical properties of the printed composite lamina

In Section 3.2, the mechanical properties of the printed composite lamina are obtained using unidirectional tensile tests of the printed samples. The mechanical properties of the composite morphing skin can be expressed as:

$$\begin{bmatrix} N \\ M \end{bmatrix} = \begin{bmatrix} A & B \\ B & D \end{bmatrix} \begin{bmatrix} \varepsilon^0 \\ \kappa \end{bmatrix} \tag{3}$$

$$\varepsilon^0 = \begin{bmatrix} \varepsilon_x^0 \\ \varepsilon_y^0 \\ \varepsilon_z^0 \end{bmatrix}, \kappa = \begin{bmatrix} \kappa_x \\ \kappa_y \\ \kappa_z \end{bmatrix}, N = \begin{bmatrix} N_x \\ N_y \\ N_z \end{bmatrix}, M = \begin{bmatrix} M_x \\ M_y \\ M_z \end{bmatrix} \tag{4}$$

where $[N \quad M]^T$ represents the force and moment resultant, $[\varepsilon^0 \quad \kappa]^T$ represents the middle plane strain and curvature. And, A, B, D denote the extension stiffness matrix, the coupling stiffness matrix and the bending stiffness matrix respectively, which are affected by the mechanical properties of the lamina and the lamina angle θ.

Thus, to evaluate the mechanical properties of the composite morphing skin, the mechanical properties of the composite lamina must be first determined. There are four elastic moduli to describe its properties, i.e., the longitudinal Young's modulus E_1, the transverse Young's modulus E_2, the major Poisson's ratio υ_{12} and the in-plane shear modulus G_{12}, which can be calculated by the following equations [43]

$$
\begin{aligned}
E_1 &= E_f V_f + E_m V_m \\
\frac{1}{E_2} &= \frac{V_f}{E_f} + \frac{V_m}{E_m} \\
\nu_{12} &= \nu_f V_f + \nu_m V_m \\
\frac{1}{G_{12}} &= \frac{V_f}{G_f} + \frac{V_m}{G_m}
\end{aligned}
\tag{5}
$$

where E_f, E_m, ν_f and ν_m are the Young's modulus of the fibre, the Young's modulus of the matrix, the Poisson's ratio of the fibre and the Poisson's ratio of the matrix, respectively. While the Young's modulus of the fibre material and the matrix material are provided by the supplier, these parameters are still insufficient to calculate the four elastic moduli of the lamina. Also, it is not straightforward to control the volume fraction of the fibre directly with the software of the 3D printer, which makes it difficult to estimate the elastic moduli directly.

Unidirectional tensile tests are performed to obtain the elastic moduli of the printed lamina, following standard test procedures [44, 45]. Three types of samples were manufactured with constant lamina angles of 0, ±45 and 90° , as shown in Fig. 5, and are denoted as Sample 1, Sample 2, and Sample 3 respectively. Sample 1 consisted of 6 plies of laminae with a 0-degree angle, Sample 2 consisted of 6 plies of laminae with a 90-degree angle and Sample 3 consisted of 8 symmetrical plies of laminae with ±45-degree angles. The ply thickness, affected by the diameter of the fibre filament, was fixed at 0.32 mm in the current study. As shown in Fig. 5, the tensile tests were conducted using a WANCE® test machine. The load cell used to measure the tensile forces had a maximum test force 50 kN and accuracy of 0.5%. A HAYTHAM® Digital Image Correlation (DIC) system was used to measure the strain distribution in the samples. The resolution of the DIC camera was 2448×2048, and the tracking speed of the pixels can achieve 1000 mm/min.

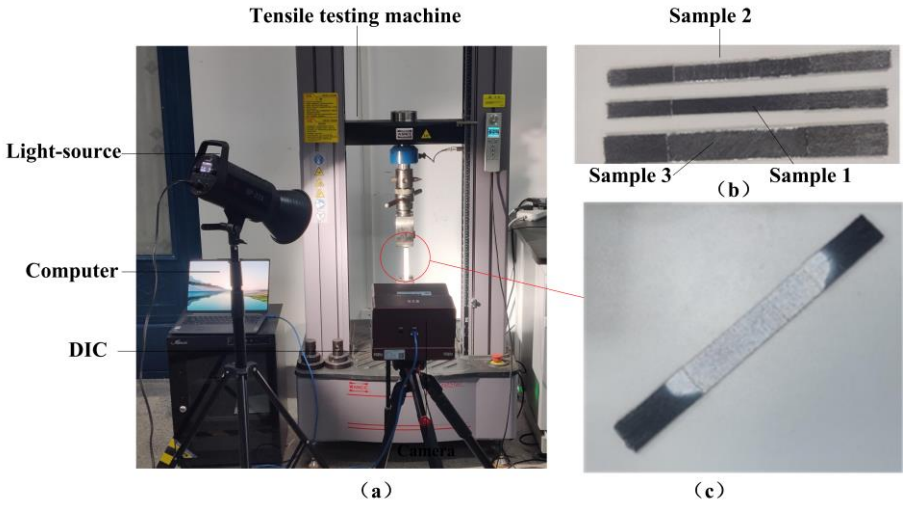

Fig. 4 (a) Facilities for the tensile tests; (b) the test samples; (c) a test sample with speckles sprayed onto the surface for DIC measurement

Three specimens of Sample 1, Sample 2 and Sample 3 were printed and tested to obtain the elastic moduli of the lamina. The test results are summarised in Table 1. As the printing conditions were unchanged, it is assumed that the fibre volume fraction (V_f) and matrix volume fraction (V_m) remained constant.

Table 1. Test results for the unidirectional laminas

Elastic moduli	Test No.1	Test No.2	Test No.3	Mean Value
E_1/GPa	45.63	49.21	44.08	46.30
E_2/GPa	1.33	1.86	1.62	1.60
υ_{12}	0.34	0.36	0.38	0.36
G_{12}/GPa	0.66	0.74	0.64	0.68

With the material modulus E_f and E_m provided in Section 3.1, together with the test results for E_1 and E_2, the volume fraction of the fibre V_f and matrix V_m can be estimated, which is around 0.3 and 0.7 respectively. The fibre volume is lower than those made by conventional methods. However, as the focus of the current paper is the variable stiffness caused by the variable lamina angle, the effect of the variable stiffness can still be highlighted by comparing it to the samples with the constant lamina angle, and the mean value of the test results will be adopted as the elastic moduli of the printed lamina for the following numerical analysis.

4. Numerical Simulation and Optimisation

4.1 Numerical Simulation

With the lamina properties obtained in Section 3, the finite element model of the composite skin is established in the commercial software Abaqus®. In the current study, four symmetrical plies of laminae were adopted, and the skin model has the length, width and thickness of 0.1 m, 0.1 m and 0.8 mm respectively.

Figure 6 shows the lamina angle and the stack sequence. The lamina angle in Ply 1 is denoted by the expression $\theta(x)$, and Ply 2 has the opposite lamina angle $-\theta(x)$. Moreover, Ply 3 and 4 are symmetrical to Plies 1 and 2.

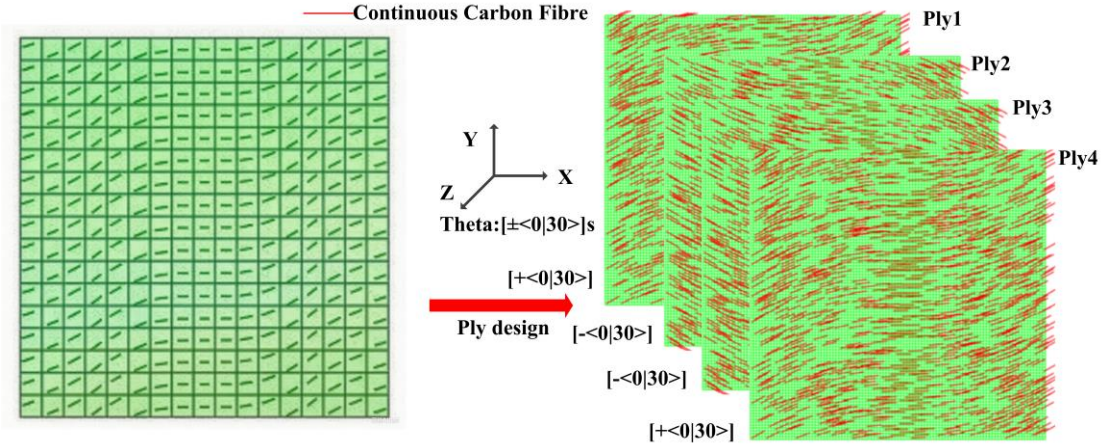

Fig. 5 (a) Finite element model of the morphing skin (b) Variation of the lamina angle in the plies

It is noted that the current layup is adopted to show the effect of the lamina angle, rather than representing practical skin design. To highlight the effect of the variable lamina angle, the composite has a symmetrical layup and the lamina angle in each layer follows the curvilinear expression in Equation (1). Considering the geometry of the skin, the general-purpose shell element S4R is used and the mesh size is 1 mm. According to Equation (1), the lamina angle varies along the x axis. In the model, the lamina angle at different locations can be calculated first, and then the lamina angle at the corresponding element can be obtained discretely, and assigned to the element by editing the input file of the finite element model with Python scripts.

Two load cases were performed to investigate the in-plane and out-of-plane mechanical properties. The first load case involved in-plane tension, with the boundary conditions shown in Fig. 3(a). A tensile displacement, corresponding to 4% overall strain of the skin, was applied to one end, and the required actuation force was obtained by summing the reaction forces at the fixed end.

Figure 7(a) shows the relationship between the parameters T_0, T_1 and the required actuation force. When the fibre direction is aligned with the morphing direction, the composite stiffness increases significantly. Consequently, when the design parameters T_0 and T_1 are close to 0°, the required actuation force is higher than when the design parameters close to 90 °. As shown in Fig. 7(a), when T_0 varies from 0 ° to 90 ° with T_1 fixed, the actuation force decreases. With an appropriate selection of T_0 and T_1, the actuation force can be reduced compared to the baseline design.

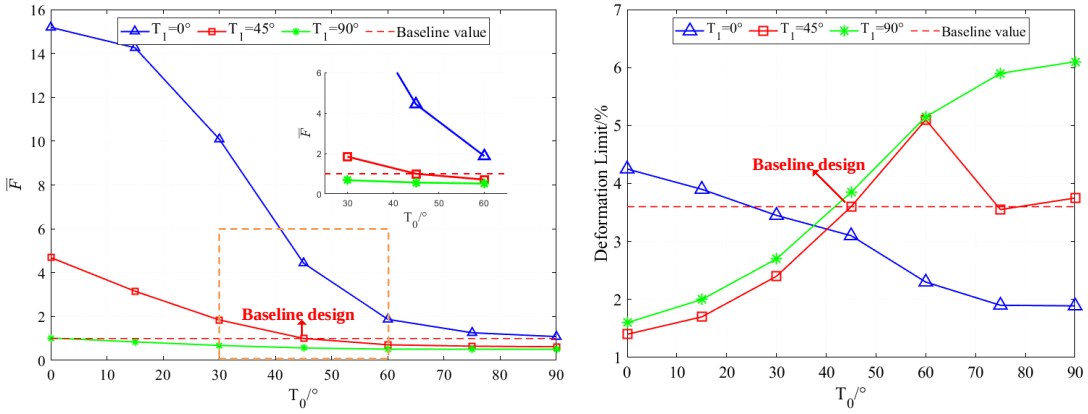

(a) Change of the required actuation force (b) Change of the deformation limit

Fig. 6 Relationship between the lamina angle parameters and: (a) required actuation force, (b) the deformation limit

The deformation limit, beyond which the skin fails, was also obtained from the in-plane tension simulation. In the current study, the Tsai-Wu criterion [46] was used to assess failure. The strength parameters of the composite are summarised in Table 2. It should be noted that the deformation limit is provided as a reference to demonstrate the effect of varying the lamina angle; therefore, the strength parameters from [47] are applied rather than those obtained from the tensile test results.

Table 2. The strength parameters of the composite from[47]

Variable	Definition	Value
X_T	Tensile strength along the fibre direction	2070 MPa
X_c	Compressive strength along the fibre direction	1360 MPa
Y_T	Tensile strength perpendicular to the fibre direction	102 MPa
Y_c	Compressive strength perpendicular to the fibre direction	276 MPa
S	Fibre shear strength	186 MPa

Figure 7(b) shows the relationship between the deformation limit and the design parameters s T_0 and T_1. The results show that varying the lamina angle also affects the deformation limit, which tends to increase when T_0 is close to T_1.

A second load case was simulated to determine the out-of-plane displacement of the morphing skin. The skin model is clamped around its four edges. A uniform pressure of 10 kPa pressure was applied to the skin surface. The maximum out-of-plane displacement was obtained and non-

dimensionalised using the result from the baseline design. Figure 8 shows the relationship between the maximum out-of-plane displacement and the lamina angle parameters.

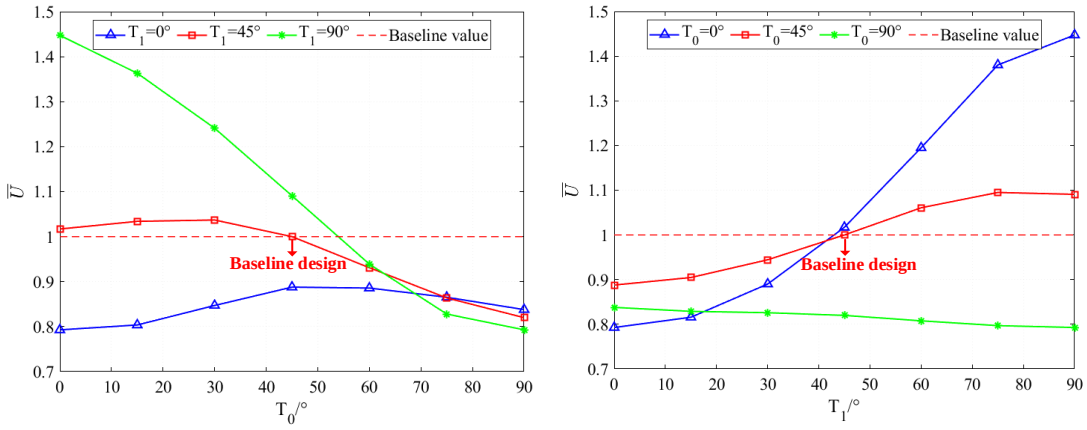

(a) Change of the maximum out-of-plane displacement with the variation of T_0

(b) Change of the maximum out-of-plane displacement with the variation of T_1

Fig. 7 Relationship between the maximum out-of-plane displacement and the lamina angle parameters with the variation of (a)T_0 and (b)T_1

With appropriate design of the parameters T_0 and T_1, the maximum out-of-plane displacement can be reduced compared to the baseline design, indicating that the lamina angle parameters have a significant effect on the out-of-plane displacement. For example, the maximum out-of-plane displacement of the layup $[\pm<0|90>]_S$ is almost twice to the layup $[\pm<90|0>]_S$, which further highlights the need to optimise the lamina angle parameters.

4.2 Skin Optimisation

A two-objective optimisation of the morphing skin was performed to calculate the Pareto front of the morphing skins. The objectives were the non-dimensionalised indexes as

$$G(x) = \min \left[\overline{F} \quad \overline{U} \right] \tag{6}$$

The maximum Tsai-Wu failure index was chosen as the constraint and was required be less than 1. Since the current study is focused on the effect of varying lamina angle, only the parameters related to the fibre lamina angle is optimised with the other parameters, such as the ply thickness kept constant. The ranges of the design variables are summarised in Table 3.

Table 3. The range of the design variables

	Number of layers	Design variable	Lower limit	Upper limit
Case 1	4	T_0^i， T_1^i (i=1)	0°	90°
Case 2	16	T_0^i， T_1^i (i=1, 2, 3, 4)	0°	90°

Two optimisation cases with different number of layers are performed. And the stacking sequence of a symmetric composite plate with 4n ply layers is denoted as $[\pm<T_0^i\,|\,T_1^i>_n]_s$ (i=1,2…n) with the superscript i used to represent the different layers.

In Case 1, four layers are applied with the lamina angle $[\pm<T_0^i\,|\,T_1^i>_n]_s$ (i=1) as shown in Fig. 6 and two design variables, i.e., T_0^1 and T_1^1, are optimised. In Case 2, 16 layers are applied with the

stacking sequence $[\pm<T_0^i\,|\,T_1^i>_n]_s$ (i=1,2,3,4) and eight design variables i.e., T_0^i and T_1^i (i=1, 2, 3, 4) are optimised.

In the current study, the two-objective optimisation is carried out using the Non-dominated Sorting Genetic Algorithm II(NSGA-II) in Matlab®. The optimisation parameters were adjusted by iteration, after which the population size, max generation crossover fraction and function convergence percentage are set to 100, 200, 0.8 and 0.01%, respectively. Python scripts are used to modify the finite element model from Section 4.1 and read the analysis results in Abaqus®.

The Pareto front obtained is shown in Fig. 9. The x axis corresponds to the required actuation force and the y axis corresponds to the maximum out-of-plane displacement. The results indicate that when the required actuation force is reduced, which is beneficial for the actuation, the out-of-plane displacement is increased, which means its capability of load-carrying is reduced. Thus, the final decision of the design parameters should be made according to the working conditions.

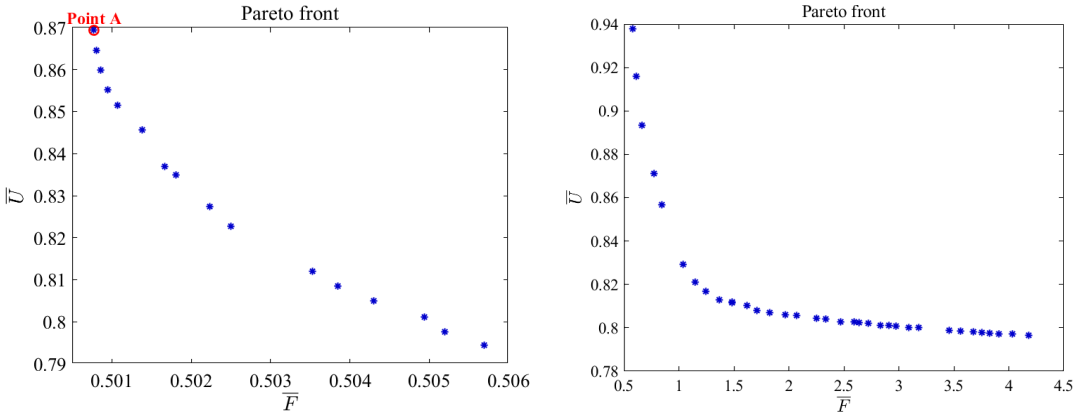

Fig. 8 Pareto front from the optimisation: (a) Case 1 with 4 layers, (b) Case 2 with 16 layers

In both cases, the effect of the varying the lamina angle is shown. In Case 1, the change of the skin performance is relatively small compared to that in Case 2, which can be due to the small number of layers, resulting a reduced number of design variables.

Considering the limitation of the manufacturing facilities, Point A is selected as an example in Fig. 9(a) for further experimental study, which has the smallest required force and highest out-of-plane displacement, but its out-of-plane displacement of the morphing skin is still less than that of the constant stiffness skin. The results of the selected point are summarised in Table 4. Since the current optimisation study is only a case study and practical applications will be explored by including more design variables and even changing the matrix material to flexible material for a high deformation limit.

Table 4. Selected point for manufacturing and testing

Parameters	$\overline{F}$(Point A)	$\overline{U}$(Point A)	T_0^1 (Point A)	T_1^1 (Point A)
Optimised results	0.5007	0.8693	70°	80°

5. Experimental Validation

The skin samples are manufactured according to the optimised design result in Section 4.2. The variation of the lamina angle was achieved by editing the corresponding G-code files of the 3D

printer. Two groups of skin samples were manufactured for the in-plane and out-of-plane tests respectively, with each group containing one sample with curved fibre and one sample with straight fibre as the baseline design. in total, four skin samples printed, as summarised in Table 5.

It is true that the performance of the baseline design may be further improved by optimising its lamination parameters, and thus the performance change between the baseline design and the design with varying lamina angle may be reduced. As a case study, the focus of the current experiments is mainly to show the change of the skin performance by introducing the varying the lamina angle.

Table 5. Summary of the experimental samples

Test Samples	Layup
In-plane test: variable angle	$[\pm\langle 70\|80\rangle]_S$
In-plane test: straight fibre	$[\pm 45]_S$
Out-of-plane test: variable angle	$[\pm\langle 70\|80\rangle]_S$
Out-of-plane test: straight fibre	$[\pm 45]_S$

The test region is 100×100 mm; however, an additional region with straight fibres was printed simultaneously to allow clamping of the sample. All test samples consisted of 4 plies, each with the thickness of 0.2 mm. Figure 10 shows the test samples and the corresponding fibre paths, including additional region printed for clamping.

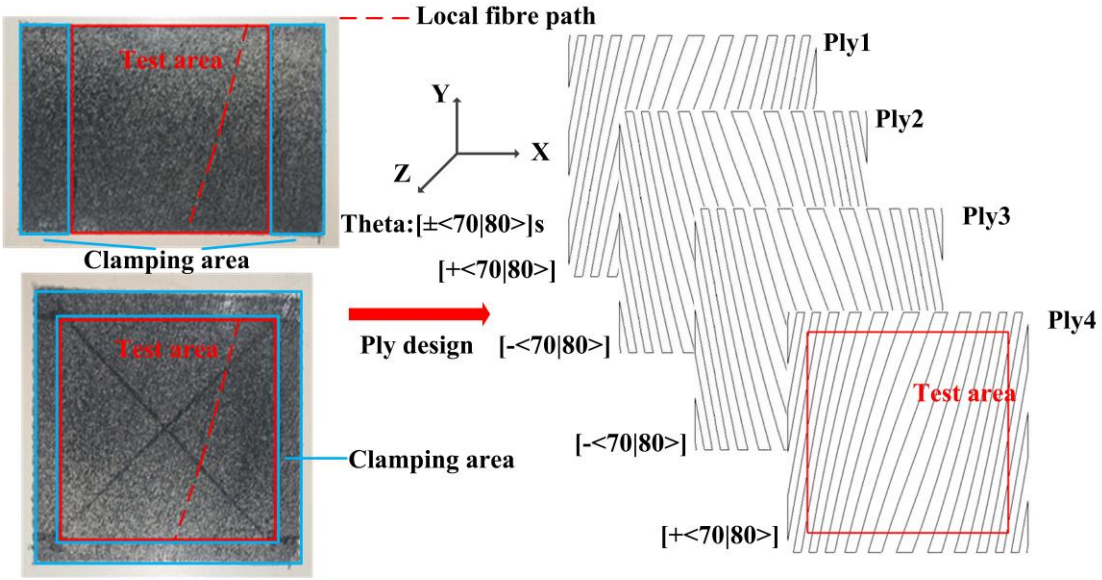

Fig. 9 Morphing skin test samples and the corresponding fibre paths

Both the in-plane tension stiffness and the out-of-plane stiffness of the samples were measured experimentally. The in-plane test were caried out using a WANCE TSE504C test machine. As the sample width was 100 mm, a customed fixture was used to clamp the specimen, as shown in Fig. 11(a). Both the variable angle and straight fibre samples were tested, and the corresponding force-displacement curves are presented in Fig. 11(b). The in-plane tensile stiffness was obtained from the slope of the curve.

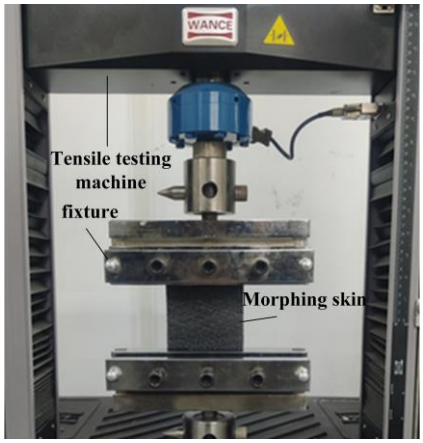

(a)Tensile experimental platform

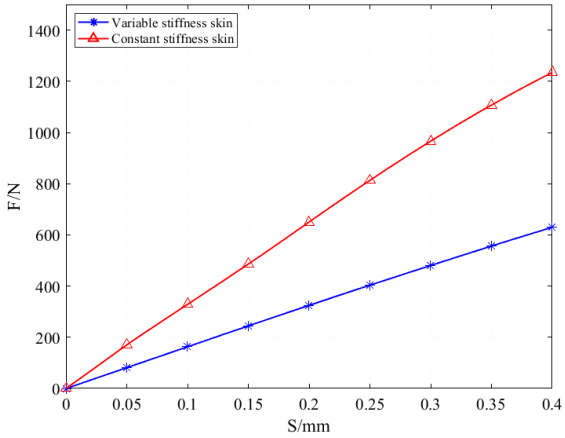

(b) Tensile test results

Fig. 10 In-plane deformation experiment

Clearly, the variable angle sample exhibited much lower in-plane tensile stiffness than the straight fibre. A 46.9% reduction was observed, from 2860 N/mm to 1520 N/mm, demonstrating a significant improvement for the morphing skin.

The out-of-plane displacement was measured by placing weights onto the test samples, which were clamped along all four edges, as shown in Fig. 12(a). To apply the out-of-plane loads evenly onto the skin sample, the weight were placed inside a square box of the same size as the test region of the skin, filled with iron spheres and weights inside the box. A laser displacement sensor was used to measure the out-of-plane displacement at the centre of the test sample. Figure 12(b) shows the curve of the out-of-plane displacement when weights are applied continuously from 1 to 5 kg. And the out-plane stiffness is obtained by calculating the slope of the curve.

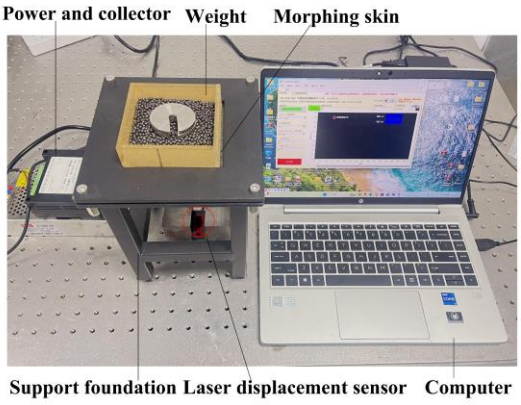

(a) Out-of-plane deformation test platform

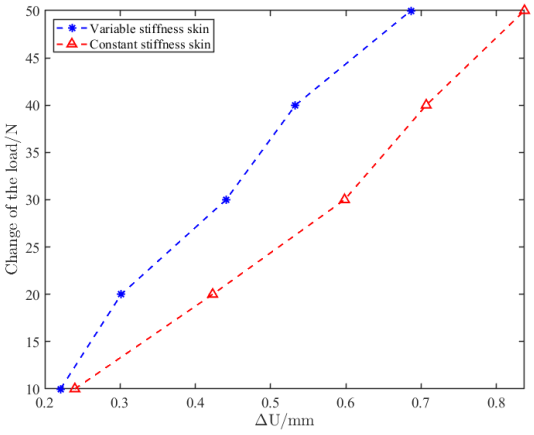

(b) Out-of-plane deformation test results

Fig. 11 In-plane deformation experiment

The variable angle sample has a higher out-of-plane stiffness than the straight fibre sample. It is found that the out-of-plane stiffness is increased from 66.7 N/mm to 85.5 N/mm, representing a 28.2% improvement through the variation of the lamina angle.

The test results for variable angle samples were also compared with the numerical results obtained in Section 4. As shown in Table 5, the differences between the experimental results and the numerical results are less than 15%, which also shows the validity of the modelling method

preliminarily. The errors could be due to the uncertainties during the 3D printing, which may affect the material properties.

Table 6. Comparison of experimental and numerical results

	Experimental results	Numerical results	Relative error
Tension stiffness	1520 N/mm	1310 N/mm	13.7%
Out-of-plane stiffness	85.5 N/mm	92.2N/mm	7.3%

6. Conclusions

This study investigated the design and fabrication of morphing skins using continuous fibre 3D printing, with variable stiffness introduced through curvilinear fibre paths defined by a lamina angle function $\theta(x)$ governed by parameters T_0 and T_1. Numerical modelling, optimisation, and experimental validation were carried out to evaluate the feasibility and performance of this approach. The main conclusions are:

1. A finite element model of the morphing skin with curvilinear lamina angle distributions was established. Parametric analysis confirmed that the stiffness of the morphing skin can be tuned effectively by adjusting the T_0 and T_1, parameters in the curvilinear function $\theta(x)$.
2. A two-objective optimisation was performed, balancing actuation force and out-of-plane stiffness. A representative Pareto-optimal design was selected, fabricated, and tested, demonstrating the practicality of the curvilinear fibre design.
3. Experimental results showed that the curvilinear-fibre specimens exhibited a 46.9% reduction in in-plane stiffness and a 28.2% increase in out-of-plane stiffness compared with straight-fibre baselines. These findings demonstrate the significant performance gains achievable by tailoring curvilinear fibre paths.
4. The close agreement between simulation and experimental results (errors <15%) validates the modelling approach and confirms that continuous fibre 3D printing can reliably realise curvilinear fibre architectures that are challenging to achieve using conventional methods.

Overall, the results highlight that continuous fibre 3D printing enables the design of morphing skins with spatially varying stiffness achieved through curvilinear fibre paths. This provides a powerful and flexible approach for tailoring actuation and load-carrying requirements in morphing aircraft. Future studies should focus on extending classical laminate plate theory to better capture the mechanics of curvilinear laminates, exploring additional optimisation variables such as ply thickness and number of layers, and integrating the morphing skin design with internal structures. Ultimately, full-scale morphing wing demonstrators will be developed to validate the benefits of curvilinear fibre designs in realistic flight scenarios.

Declaration of competing interest

The authors declare that they have no known competing financial interests or personal relationships that could have appeared to influence the work reported in this paper.

Acknowledgments

The first four authors would like to acknowledge the funding from National Natural Science Foundation of China (Grant No. 52305262) and the Starting Grant of Nanjing University of Aeronautics and Astronautics (Grant No. YQR22056).

Data Availability

The data that support the findings of this study are available from the corresponding author upon reasonable request.

References

1. Barbarino, S., O. Bilgen, R.M. Ajaj, M.I. Friswell, and D.J. Inman, *A review of morphing aircraft.* Journal of Intelligent Material Systems and Structures, 2011. 22(9): p. 823-877.
2. Li, D., S. Zhao, A. Da Ronch, J. Xiang, J. Drofelnik, Y. Li, L. Zhang, Y. Wu, M. Kintscher, H.P. Monner, A. Rudenko, S. Guo, W. Yin, J. Kirn, S. Storm, and R.D. Breuker, *A review of modelling and analysis of morphing wings.* Progress in Aerospace Sciences, 2018. 100: p. 46-62.
3. Thill, C., J. Etches, I. Bond, K. Potter, and P. Weaver, *Morphing skins.* The Aeronautical Journal, 2008. 112(1129): p. 117-139.
4. Ahmad, D., M.S. Parancheerivilakkathil, A. Kumar, M. Goswami, R.M. Ajaj, K. Patra, M. Jawaid, K. Volokh, and Y. Zweiri, *Recent developments of polymer-based skins for morphing wing applications.* Polymer Testing, 2024. 135: p. 108463.
5. Sun, J., Q. Guan, Y. Liu, and J. Leng, *Morphing aircraft based on smart materials and structures: A state-of-the-art review.* Journal of Intelligent Material Systems and Structures, 2016. 27(17): p. 2289-2312.
6. Chen, S., Y. Chen, Z. Zhang, Y. Liu, and J. Leng, *Experiment and analysis of morphing skin embedded with shape memory polymer composite tube.* Journal of Intelligent Material Systems and Structures, 2014. 25(16): p. 2052-2059.
7. Ren, X. and G. Zhu, *A variable stiffness morphing skin: preparation and properties.* Smart Materials and Structures, 2021. 30(12): p. 125016.
8. Sun, J., L. Du, F. Scarpa, Y. Liu, and J. Leng, *Morphing wingtip structure based on active inflatable honeycomb and shape memory polymer composite skin: A conceptual work.* Aerospace Science and Technology, 2021. 111: p. 106541.
9. Vos, R. and R. Barrett, *Mechanics of pressure-adaptive honeycomb and its application to wing morphing.* Smart Materials and Structures, 2011. 20(9): p. 094010.
10. Meyer, P., H. Traub, and C. Hühne, *Actuated adaptive wingtips on transport aircraft: Requirements and preliminary design using pressure-actuated cellular structures.* Aerospace Science and Technology, 2022. 128: p. 107735.
11. Meyer, P., M. Vorhof, J. Koord, C. Sennewald, C. Cherif, and C. Hühne, *Anisotropic flexure hinges: Manufacturing and mechanical characterization for application in pressure-actuated morphing structures.* Composites Part B: Engineering, 2023. 266: p. 110967.
12. Bubert, E.A., B.K. Woods, K. Lee, C.S. Kothera, and N.M. Wereley, *Design and fabrication of a passive 1D morphing aircraft skin.* Journal of Intelligent Material Systems and Structures, 2010. 21(17): p. 1699-1717.
13. Olympio, K.R. and F. Gandhi, *Optimal Cellular Core Topologies for One-Dimensional Morphing Aircraft Structures.* Journal of Mechanical Design, 2012. 134(8): p. 081005-081005-10.
14. Liu, W., H. Li, Z. Yang, J. Zhang, and C. Xiong, *Mechanics of a novel cellular structure for morphing applications.* Aerospace Science and Technology, 2019. 95: p. 105479.
15. Schmitz, A. and P. Horst, *Bending deformation limits of corrugated unidirectionally reinforced composites.* Composite Structures, 2014. 107: p. 103-111.
16. Dayyani, I., A.D. Shaw, E.I. Saavedra Flores, and M.I. Friswell, *The mechanics of composite corrugated structures: A review with applications in morphing aircraft.* Composite Structures, 2015. 133: p. 358-380.
17. Shaw, A.D., I. Dayyani, and M.I. Friswell, *Optimisation of composite corrugated skins for buckling in morphing aircraft.* Composite Structures, 2015. 119: p. 227-237.

18. Wang, C., Y. Xia, M.I. Friswell, and E.S. Flores, *Predicting global strain limits for corrugated panels.* Composite Structures, 2020. 231: p. 111472.
19. Vasista, S., F. Nolte, H.P. Monner, P. Horst, and M. Burnazzi, *Three-dimensional design of a large-displacement morphing wing droop nose device.* Journal of Intelligent Material Systems and Structures, 2018. 29(6): p. 3222-3241.
20. De Gaspari, A., V. Cavalieri, and S. Ricci, *Experimental and performance validation of a full-scale morphing droop nose design based on composite compliant structures.* Composite Structures, 2024. 348: p. 118502.
21. Thuwis, G.A.A., M.M. Abdalla, and Z. Gürdal, *Optimization of a variable-stiffness skin for morphing high-lift devices.* Smart Materials and Structures, 2010. 19(12): p. 124010.
22. Wang, C., H. Haddad Khodaparast, M.I. Friswell, A. Magrini, R. Ponza, E. Benini, V. Landersheim, D. Laveuve, and C. Contell Asins, *Conceptual-level evaluation of a variable stiffness skin for a morphing wing leading edge.* Proceedings of the Institution of Mechanical Engineers, Part G: Journal of Aerospace Engineering, 2019. 233(15): p. 5703-5716.
23. Lopes, C.S., Z. Gürdal, and P.P. Camanho, *Variable-stiffness composite panels: Buckling and first-ply failure improvements over straight-fibre laminates.* Computers & Structures, 2008. 86(9): p. 897-907.
24. Sabido, A., L. Bahamonde, R. Harik, and M.J.L. van Tooren, *Maturity assessment of the laminate variable stiffness design process.* Composite Structures, 2017. 160: p. 804-812.
25. Kim, B.C., K. Potter, and P.M. Weaver, *Continuous tow shearing for manufacturing variable angle tow composites.* Composites Part A: Applied Science and Manufacturing, 2012. 43(8): p. 1347-1356.
26. Vijayachandran, A.A., P. Davidson, and A.M. Waas, *Optimal fiber paths for robotically manufactured composite structural panels.* International Journal of Non-Linear Mechanics, 2020. 126: p. 103567.
27. Punera, D. and P. Mukherjee, *Recent developments in manufacturing, mechanics, and design optimization of variable stiffness composites.* Journal of Reinforced Plastics and Composites, 2022. 41(23-24): p. 917-945.
28. Kabir, S.M.F., K. Mathur, and A.-F.M. Seyam, *A critical review on 3D printed continuous fiber-reinforced composites: History, mechanism, materials and properties.* Composite Structures, 2020. 232: p. 111476.
29. Tian, X., A. Todoroki, T. Liu, L. Wu, Z. Hou, M. Ueda, Y. Hirano, R. Matsuzaki, K. Mizukami, K. Iizuka, A.V. Malakhov, A.N. Polilov, D. Li, and B. Lu, *3D Printing of Continuous Fiber Reinforced Polymer Composites: Development, Application, and Prospective.* Chinese Journal of Mechanical Engineering: Additive Manufacturing Frontiers, 2022. 1(1): p. 100016.
30. Catapano, A., M. Montemurro, J.-A. Balcou, and E. Panettieri, *Rapid Prototyping of Variable Angle-Tow Composites.* Aerotecnica Missili & Spazio, 2019. 98(4): p. 257-271.
31. Chen, Z., Z. Zhang, K. Granland, C. Chen, and Y. Tang, *Exploring optimal adaptive process parameters for curved infill paths of additive manufactured carbon fibre reinforced polymers.* Composites Communications, 2023. 39: p. 101549.
32. Le Duigou, A., M. Grabow, M. Castro, R. Toumi, M. Ueda, R. Matsuzaki, Y. Hirano, J. Dirrenberger, F. Scarpa, R. D'Elia, K. Labstie, and U. Lafont, *Thermomechanical performance of continuous carbon fibre composite materials produced by a modified 3D printer.* Heliyon, 2023. 9(3): p. e13581.
33. Dong, K., T. Hou, P. Zheng, and Y. Xiong, *Continuous fiber-reinforced 2.5D hybrid lattice structures with superior compression performance via self-supporting suspension printing.* Composites Science and Technology, 2024. 257: p. 110845.

34. Sugiyama, K., R. Matsuzaki, M. Ueda, A. Todoroki, and Y. Hirano, *3D printing of composite sandwich structures using continuous carbon fiber and fiber tension.* Composites Part A: Applied Science and Manufacturing, 2018. 113: p. 114-121.
35. Cheng, P., Y. Peng, S. Li, Y. Rao, A. Le Duigou, K. Wang, and S. Ahzi, *3D printed continuous fiber reinforced composite lightweight structures: A review and outlook.* Composites Part B: Engineering, 2023. 250: p. 110450.
36. Fallah, A., S. Asif, G. Gokcer, and B. Koc, *4D printing of continuous fiber-reinforced electroactive smart composites by coaxial additive manufacturing.* Composite Structures, 2023. 316: p. 117034.
37. Wang, Y., H. Ye, J. He, Q. Ge, and Y. Xiong, *Electrothermally controlled origami fabricated by 4D printing of continuous fiber-reinforced composites.* Nature Communications, 2024. 15(1): p. 2322.
38. Heeb, R.M., M. Dicker, and B. K S Woods, *Manufacturing and characterisation of 3D printed thermoplastic morphing skins.* Smart Materials and Structures, 2022. 31(8): p. 085007.
39. Murugan, S. and M.I. Friswell, *Morphing wing flexible skins with curvilinear fiber composites.* Composite Structures, 2013. 99: p. 69-75.
40. Anisoprint. *Product Manual of the Anisoprint Composer A4 printer* 2024]; Available from: https://anisoprint.com/.
41. Liu, F., E. Ferraris, and J. Ivens, *Mechanical investigation and microstructure performance of a two-matrix continuous carbon fibre composite fabricated by 3D printing.* Journal of Manufacturing Processes, 2022. 79: p. 383-393.
42. Fallah, A., Q. Saleem, and B. Koc, *Assessment of mechanical properties and shape memory behavior of 4D printed continuous fiber-reinforced PETG composites.* Composites Part A: Applied Science and Manufacturing, 2024. 181: p. 108165.
43. Kaw, A.K., *Mechanics of composite materials*. Second ed. 2010, Boca Raton: CRC press.
44. ASTM International, *ASTM D3039/D3039M-17 Standard Test Method for Tensile Properties of Polymer Matrix Composite Materials*. 2017: West Conshohocken, PA, USA.
45. ASTM International, *ASTM D3518/D3518M-18 Standard Test Method for In-Plane Shear Response of Polymer Matrix Composite Materials by Tensile Test of a ± 45°Laminate.* 2018: West Conshohocken, PA, USA.
46. Tsai, S.W. and E.M. Wu, *A general theory of strength for anisotropic materials.* Journal of composite materials, 1971. 5(1): p. 58-80.
47. Liu, H., J. Liu, Y. Ding, Z.E. Hall, X. Kong, J. Zhou, B.R.K. Blackman, A.J. Kinloch, and J.P. Dear, *A three-dimensional elastic-plastic damage model for predicting the impact behaviour of fibre-reinforced polymer-matrix composites.* Composites Part B: Engineering, 2020. 201: p. 108389.

Declaration of competing interest

The authors declare that they have no known competing financial interests or personal relationships that could have appeared to influence the work reported in this paper.

Acknowledgments

The first four authors would like to acknowledge the funding from National Natural Science Foundation of China (Grant No. 52305262) and the Starting Grant of Nanjing University of Aeronautics and Astronautics (Grant No. YQR22056).